

DRAFT

CMS Physics Analysis Summary

The content of this note is intended for CMS internal use and distribution only

2015/10/26

Head Id: 297494

Archive Id: 304805:305633M

Archive Date: 2015/07/21

Archive Tag: trunk

Search for New Physics in the V/jet + MET final state

The CMS Collaboration

Abstract

A search is presented for an excess of events with a high energy jet in association with a large missing transverse momentum in a data sample of proton-proton interactions at centre-of-mass energy of 8TeV. The data correspond to an integrated luminosity of 19.7 fb^{-1} collected by the CMS detector at the LHC. Additional sensitivity is achieved by tagging events consistent with the jet originating from a hadronically decaying vector boson. Limits are obtained on the branching ratio of a standard model Higgs boson decaying invisibly. The search is also interpreted in terms of dark matter production to place constraints on the parameter space of simplified models.

This document has been revised with respect to the version dated July 20, 2015.

This box is only visible in draft mode. Please make sure the values below make sense.

PDFAuthor: CMS Collaboration
PDFTitle: Search for New Physics in the V/jet + MET final state
PDFSubject: CMS
PDFKeywords: CMS, physics, software, computing

Please also verify that the abstract does not use any user defined symbols

1 Introduction

Dark matter (DM) is one of the most compelling pieces of indirect evidence for physics beyond the Standard Model (SM). In many DM theories, the collider production of particle DM proceeds via a mediator with couplings to the SM. The canonical “monojet” search strategy provides a model-independent means of exploring this scenario [1, 2] while related “mono-V” ($V=W/Z$) searches [3–7] target the associated production of DM with SM vector bosons, which can be enhanced in theories with non-universal DM couplings [8]. The interpretation of results from these and other DM searches at the Large Hadron Collider (LHC) have generally utilized effective field theories (EFT) that assume heavy mediators and DM production via contact interactions [9].

The analysis described is a search for new physics containing an energetic jet and an imbalance in transverse momentum (E_T^{miss}) using the full 8 TeV dataset from Run-1 corresponding to an integrated luminosity of 19.7 fb^{-1} . The search is the first at CMS to target the hadronic decay modes of the vector bosons in the mono-V channels. A multivariate V-tagging technique is employed to identify the individually resolved decay products of moderately boosted vector bosons. The exploration of mono-V production at high boost utilises recently developed techniques designed to exploit information available in the sub-structure of jets. The analysis incorporates both monojet and mono-V final states in a combined search, categorized according to the nature of the jets in the event. The DM signal extraction is performed by considering the shape of the E_T^{miss} distribution in each event category, which provides improved sensitivity compared to the previous CMS monojet analysis [1].

The results are interpreted using simplified DM models, which are most appropriate when considering DM mediator production [10, 11], which span a broad range of mediator and DM particle properties. Where previous searches have provided interpretations using an EFT based approach, in light of recent developments, this analysis focuses on the use of the simplified models scheme for which a mediator and coupling are well defined [12].

This note is structured as follows; a brief description of the CMS detector is presented in Section 2, Section 3 outlines details of the simulation used in the analysis and Section 4 provides a description of the physics object reconstruction and the event selection and categorisation. Section 5 describes the background modelling used in the signal extraction. The results of this approach are given in Section 6, while interpretations of the results in the context of DM are presented in Section 7.

2 CMS detector

The CMS detector, described in detail in ref. [13], is a multi-purpose apparatus designed to study high- p_T physics processes in proton-proton and heavy-ion collisions. A superconducting solenoid occupies its central region, providing a magnetic field of 3.8 T parallel to the beam direction. Charged-particle trajectories are measured by the silicon pixel and strip trackers, which cover a pseudorapidity region of $|\eta| < 2.5$. A lead tungstate (PbWO_4) crystal electromagnetic calorimeter (ECAL) and a brass/scintillator hadron calorimeter (HCAL) surround the tracking volume and cover $|\eta| < 3$. The steel/quartz-fiber Cherenkov hadron forward (HF) calorimeter extends the coverage to $|\eta| < 5$. The muon system consists of gas-ionization detectors embedded in the steel flux return yoke outside the solenoid, and covers $|\eta| < 2.4$. The first level of the CMS trigger system, composed of custom hardware processors, is designed to select the most interesting events in less than $4 \mu\text{s}$, using information from the calorimeters and muon detectors. The high-level trigger processor farm then further reduces the event rate to a

few hundred Hz.

3 Monte Carlo Simulation

The signature of monojet and hadronic mono-V production is a large value of missing E_T^{miss} recoiling against jets. The largest backgrounds are due to Z+jet production in which the Z decays to neutrinos, and leptonically decaying W+jet production where the charged lepton falls outside of the detector acceptance or fails the reconstruction criteria, thus producing real E_T^{miss} .

Simulated events are used throughout the analysis to determine both the expected signal and background contributions. Where possible, data-driven corrections are applied to the simulation so that it more accurately describes the data. The Z+jets, W+jets, $t\bar{t}$ and QCD background Monte Carlo (MC) samples are produced using Madgraph [14] interfaced with Pythia6 [15] for hadronization and fragmentation, where jets from the matrix element are matched to the parton shower following the MLM matching prescription [16]. The single-top background sample is generated with POWHEG [17], whereas diboson samples are produced directly with Pythia6. All signal and background samples are processed using Geant4 [18], providing a full simulation of the CMS detector. The MC samples are corrected to account for the distribution of the number of additional (pileup or PU) interactions observed in 2012 dataset. Both signal and background samples are additionally corrected to account for the mis-modelling of hadronic recoil in simulation following the procedure described in [19].

The production of fermionic DM is considered via both spin-0 and spin-1 mediators. In the vector/axial-vector mediator scenario, hard initial state radiation gives rise to the monojet topology (Figure 1a), while the mono-V signature results from the associated production of vector bosons (Figure 1b). The mono-V signature produced via a spin-1 mediator is modelled as a Z' boson [20], implemented in Madgraph [14], with either pure vector or pure axial-vector couplings to SM and DM fermions, while for the monojet signature MCFM [21] is used.

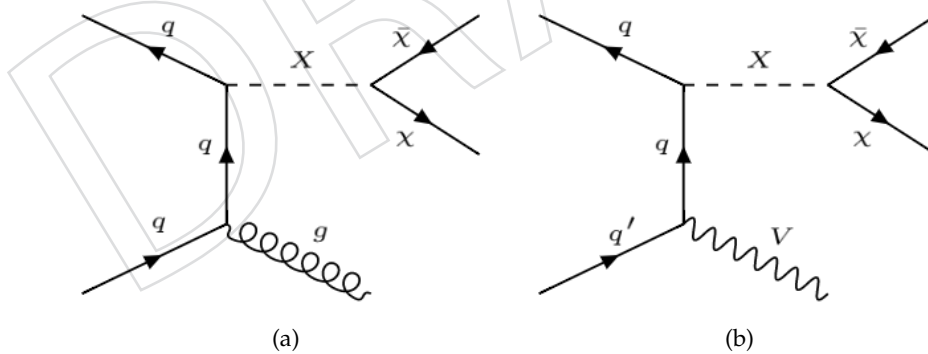


Figure 1: Diagrams for the monojet (a) and mono-V (b) processes with a spin-1 mediator.

MCFM is also used for the scalar and pseudoscalar models, shown in Figure 2. With this choice of generator, the p_T spectra are provided at leading order accuracy and with finite top mass, which has a large effect on the spectrum [22]. The mono-V signature in the scalar mediator model is generated as Higgs-strahlung (Figure 2b) with JHUGen [23], where the Higgs boson mass is modified to match the scalar mediator mass. The predicted cross-section is scaled using known next-to-next-to-leading order (NNLO) k-factors [24].

In the scalar and pseudoscalar scenarios, Yukawa couplings ($g_{SM} = g_q m_q / v$, in which m_q is the quark mass and v is the vacuum expectation value) between the mediator and SM quarks

are assumed. The scaling parameter, g_q is assumed to be flavour-universal and set constant at $g_q = 1$. Due to this, the spin-0 mediator in the monojet channel is produced primarily through a top-quark loop (Figure 2a). For all interpretations shown, the coupling of the mediator to the DM particle, g_{DM} is assumed to be 1. The minimum mediator widths are determined from the formulae given in [25].

For the specific case where the scalar mediator is assumed to be the SM Higgs, the monojet signature is produced with POWHEG, which is tuned so that the p_T spectrum reproduce predictions at NLO [24]. Instead, the Higgs-strahlung process is produced using Pythia6 for comparison with previous Higgs invisible searches in the V-boson associated production mode at CMS [4, 26]. In all interpretations, the DM particle is assumed to be a Dirac fermion.

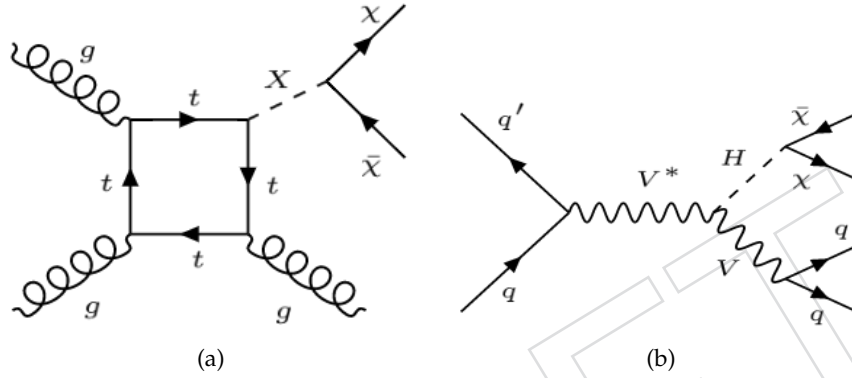


Figure 2: Diagrams for production of the monojet (a) and mono-V signature through Higgs-strahlung (b), through a scalar mediator.

4 Event Selection and Categorization

Signal events are selected on the basis of large values of E_T^{miss} and one or more high- p_T jet(s), explicitly vetoing isolated leptons and photons. The data used for this analysis are collected using two triggers designed to record events that contain a large E_T^{miss} . The first requires events for which E_T^{miss} , calculated using only information from the calorimeters, is larger than 120 GeV. The second trigger is a dedicated monojet trigger which selects events based on the amount of E_T^{miss} reconstructed using the online version of the particle-flow algorithm. Identified muons are removed from the event before the E_T^{miss} is calculated so that $Z \rightarrow \mu^+ \mu^-$ events are also selected. These events are used as a control sample for the $Z(\nu\nu) + \text{jets}$ background as described in Section 5.1. The E_T^{miss} threshold for the second trigger is 95 GeV. The E_T^{miss} threshold of this trigger is 95 GeV and 105 GeV for the first and second half of the 2012 data-taking period respectively. The threshold on the E_T^{miss} for the selection of the events is set at 200 GeV in order to maintain a high efficiency from the triggers. In addition, for the second trigger, the event is required to contain a jet with $p_T > 80$ GeV and $|\eta| < 2.6$ for which no more than 95% of the jet's energy is associated to neutral hadrons. The efficiency of these triggers is greater than 99% with respect to the full event selection.

Jets are obtained from the clustering of PF objects by means of either the anti- k_T algorithm [27] with 0.5 (ak5 jet) as the distance parameter, or the Cambridge/Aachen algorithm [28] with 0.8 distance parameter (ca8). Further selections are applied on the leading jet based on the fractions of energy associated to the PF candidate types to reduce the contribution from anomalous energy measurements. Namely, the charged hadrons fraction has to be larger than 0.2, the neutral electromagnetic fraction has to be smaller than 0.7 and the neutral hadronic fraction has to

be smaller than 0.7. Jet energies are corrected for pileup on the basis of the event energy density and proportionally to their area. Data-driven scale calibrations are then applied to correct the energy of the jets [29].

The E_T^{miss} is calculated as the magnitude of the negative vector sum of the transverse momenta of all final state particles, which are reconstructed using the particle-flow (PF) algorithm [30]. Events with a large mis-reconstructed offline E_T^{miss} are removed by applying quality filters. The angle between the E_T^{miss} and the leading jet is required to be larger than 2 to reduce the contribution from multijet QCD events. Finally, events are vetoed which contain at least one well-identified and isolated electron, photon or muon with $p_T > 10$ GeV, or a tau with $p_T > 15$ GeV.

Selected events are classified into three event categories, based on the topology of the jets, in order to distinguish between initial or final state radiation of gluons or quarks versus jets arising from hadronic vector boson decays. Events are first scrutinized for the presence of an unresolved vector boson, subsequently for a resolved vector boson and finally the remaining events are collected into the monojet category.

4.1 Unresolved (Boosted) V-tagged category

If the electroweak boson decays hadronically and it has sufficiently high transverse momentum, both its hadronic decay products are captured by a single reconstructed “fat”-jet. The selection for this category is devised to identify such events by selecting events containing a ca8 jet with a large p_T . The variable “N-subjettiness”, τ_N , defined in [31, 32], has been shown to be a powerful discriminator for hadronic V-tagging when combined into ratios τ_N/τ_{N-1} , where N is the hypothesized number of subjets. For the boosted vector boson topology, the discriminating ratio is τ_2/τ_1 . Additionally, the jet mass is used as it is the most natural discriminator between jets originating from vector boson decays and those originating from single partons. The ca8 jet mass is recomputed using a jet grooming technique to improve mass resolution by reducing the effects from pileup and underlying event. Events with $E_T^{\text{miss}} > 250$ GeV and a ca8 jet with $p_T > 200$ GeV are categorised as boosted if the jet additionally satisfies the criteria that the τ_2/τ_1 ratio is smaller than 0.5 and the pruned jet mass [33], m_{prune} , satisfies $60 < m_{\text{prune}} < 110$ GeV. Figure 3 shows the distributions of τ_2/τ_1 and m_{prune} , (before the application of the jet mass cut) in simulation and data for the boosted event category.

Events which contain additional jets close to the ca8 jet, but no closer than $\Delta R < 0.5$, are selected to include the frequent cases in which initial state radiation yields additional jets. If an ak5 jet with $p_T > 30$ and $|\eta| < 2.5$ is reconstructed, and the opening angle between it and the ca8 jet, $\Delta\phi(\text{ak5}, \text{ca8})$, is smaller than 2, the event is selected. Events with more than one ak5 jets with $p_T > 30$ GeV and $|\eta| < 2.5$, reconstructed at $\Delta R > 0.5$ with respect to the ca8 jet are rejected.

4.2 Resolved V-tagged category

In cases where the electroweak boson has insufficient transverse momentum for its hadronic decay to be fully contained in a single reconstructed fat-jet, a selection that looks for decays into a pair of ak5 jets is applied to recover the event. The selection requires that each jet has $p_T > 30$ GeV and $|\eta| < 2.5$ and that the dijet has a mass between 60 GeV and 110 GeV, consistent with originating from an electroweak boson. After such a selection, there is still a large combinatorial background of random pairing of jets from processes such as Z+jets and W+jets. To further reduce the combinatorial background, a multivariate V-tagger is applied. The inputs to this resolved V-tagger are;

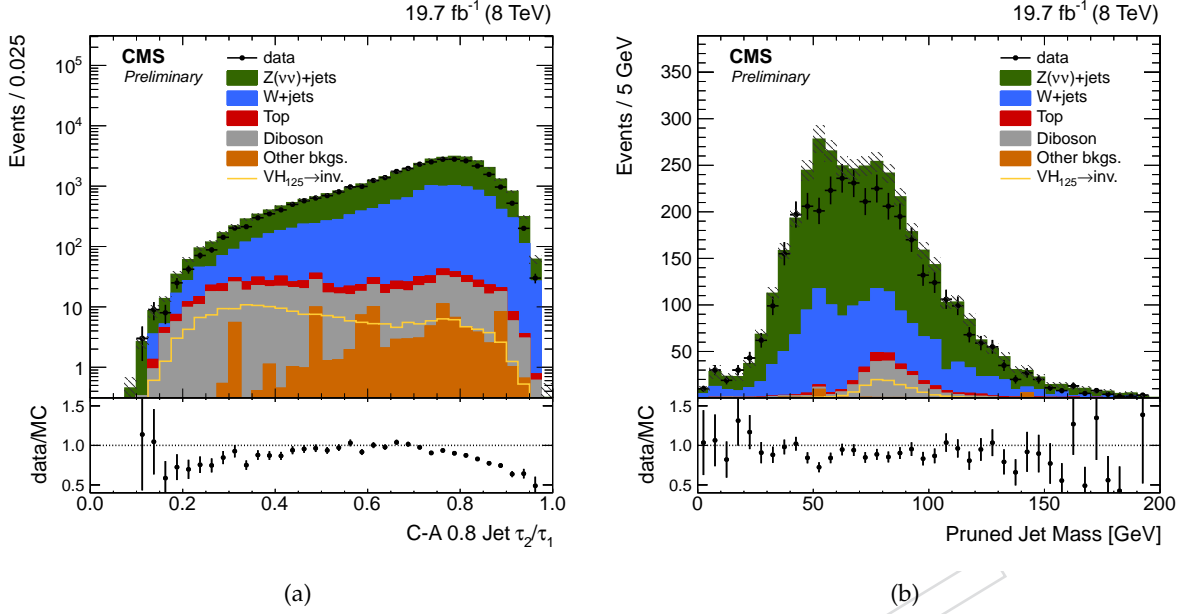


Figure 3: Distributions of τ_2/τ_1 before the jet mass cut (a) and pruned jet mass (b) for events in data and MC in the boosted event category. A cut of $\tau_2/\tau_1 < 0.5$ is applied in figure b.

- **Quark/Gluon Discriminator.** A likelihood-based discriminator that distinguishes quark-initiated jets from gluon-initiated jets. The discriminator value from both jets are provided as input to the V-tagger [34].
- **Jet Pull Angle.** The jet pull angle [35] is correlated with the color connection of a pair of jets. Since electroweak bosons are color singlets, the jets from their decays tend to have a smaller pull angle, in contrast to the combinatorial background that have no preferred angle. The pull angle of the trailing jet with respect to the leading jet and vice versa are given as input to the V-tagger.
- **Mass Drop.** The mass drop variable is defined as [36],

$$\frac{\max(m_1, m_2)}{m_{12}} \Delta R_{12},$$

where m_1 and m_2 are the masses of each jet, m_{12} is the dijet mass, and ΔR_{12} is the separation between the jets. This quantity tends to be smaller for dijets from vector boson decays compared to random pairings from background.

- **Dijet p_T/m .** Ratio of the dijet p_T to the dijet mass. This variable was found to perform better than the dijet p_T alone.

The distribution of the V-tagger variable for SM backgrounds and a Higgs boson with mass of 125 GeV produced in association with either a W or Z boson is shown in Figure 4.

To be tagged as a hadronic V-boson decay, the value of the discriminator for the event must be larger than 0.6. In events where multiple dijet pairs are found, the pair with the highest V-tagger value is taken as the candidate. To reduce contamination from top backgrounds, the event is rejected if it contains a b-tagged jet, defined using the CSV medium definition [37]. Finally, the events are required to have $E_T^{\text{miss}} > 250$ GeV to avoid the bias of the E_T^{miss} spectrum introduced from the requirements on the dijet system's transverse momentum through the application of the V-tagger.

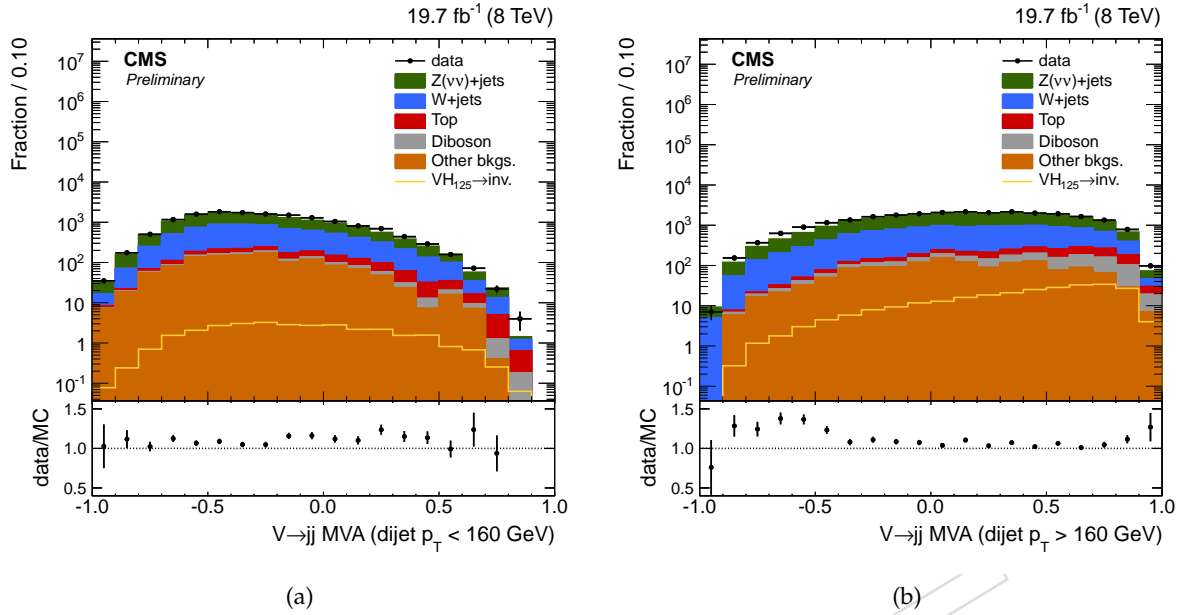


Figure 4: Resolved V-tagger variable distribution in simulation and data after all other signal region cuts in the resolved category. The distributions are shown split into dijet $p_T < 160$ GeV (a) and dijet $p_T > 160$ GeV (b), corresponding roughly to the point at which jets begin to overlap. The expected distribution for the vector boson produced in association with a Higgs boson with a mass of 125 GeV is shown.

4.3 Monojet category

The events that do not qualify for either of the two V-tagged categories are tested for the presence of a single jet originating from quark or gluon radiation. For the monojet category, at least one ak5 jet within $|\eta| < 2.0$ with p_T greater than 150 GeV and a E_T^{miss} greater than 200 GeV is required. As in the boosted category, events with a second ak5 jet close to the leading one ($\Delta\phi(j_1, j_2) < 2$) with $p_T > 30$ GeV and $|\eta| < 2.5$ are selected to allow the frequent cases where initial state radiation yields two jets. Events with three or more ak5 jets with $p_T > 30$ GeV and $|\eta| < 2.5$ are rejected.

Figure 5 shows the E_T^{miss} and leading jet p_T distributions in data and simulation after selection for all three event classes combined. The backgrounds are normalized to 19.7 fb^{-1} and the expected distribution for a Higgs boson with a mass of 125 GeV, decaying invisibly, is shown. The discrepancy between the data and simulation is a result of both mis-modelling of the detector resolution and an imperfect theoretical description of the W/Z+jet processes. Both effects are corrected for in this analysis using a data-driven approach described in the following section.

5 Signal Extraction

The presence of a signal could be revealed by an excess of events with respect to the expectations for the SM backgrounds in a region at high missing transverse energy. Significant improvements in terms of sensitivity can be expected if the shape of a discriminating variable is considered. More information is exploited to extract a possible signal, in particular the part of the spectrum where the background is dominant is used to constrain the region where the

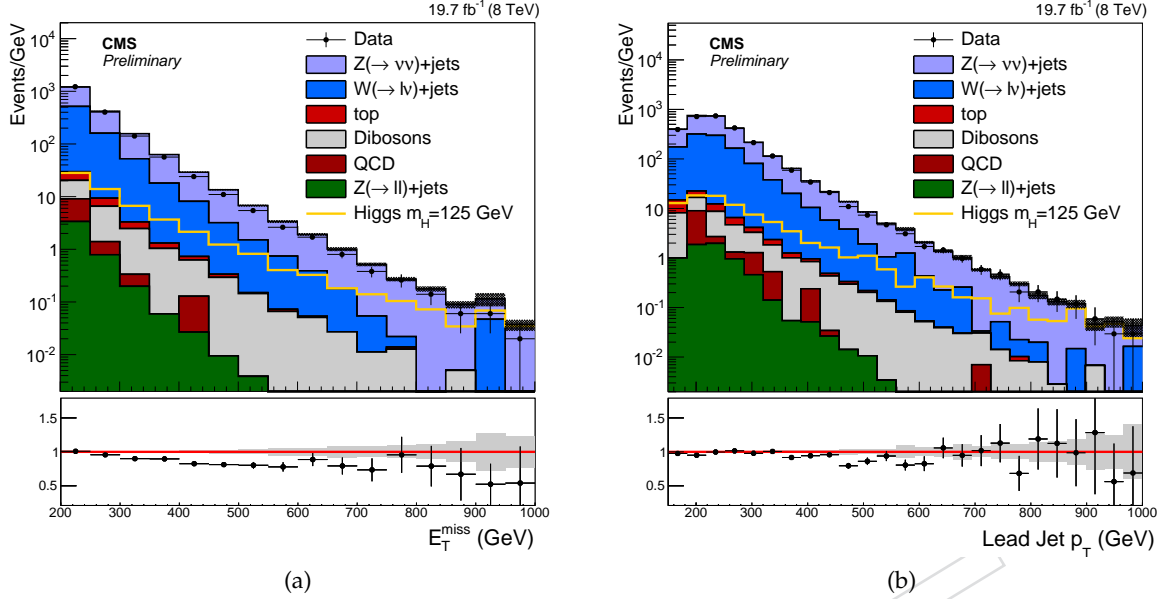


Figure 5: Distributions of E_T^{miss} (a) and leading jet p_T (b) in simulated events and data after the signal selection for all three event categories combined. The expected distribution for a Higgs boson with mass 125 GeV is shown assuming the SM Higgs cross-section and an invisible branching ratio of 100%. The gray band in the ratios indicate the statistical uncertainty from the limited number of background MC events.

signal-to-background ratio is larger. As a natural choice the E_T^{miss} distribution is chosen.

A template fit is then performed in the range 250 GeV to 1000 GeV (or 200 GeV to 1000 GeV for the monojet category), where the binning is chosen to ensure each corresponding bin of the control regions is populated. The width of the highest E_T^{miss} bin is chosen for ease of comparison to the previous CMS search [1].

5.1 W+jets and Z+jets Backgrounds

The accuracy with which the shapes for the major backgrounds (V+jets) is estimated is an essential part of this analysis. Data from control regions are utilised in order to determine both the shape and normalization for the V+jets backgrounds in the signal region. The procedure adopted is to derive a correction in bins of E_T^{miss} , using the data control regions, which can be used to re-weight the simulated V+jets events in the signal region. The events in the control regions are divided into the three categories, using the same selection criteria as described in Section 4, with exceptions which are described in the following section.

5.1.1 Control regions in data

The decays of a Z boson into a pair of muons or a pair of neutrinos are very similar from a theoretical point of view. Apart from acceptance effects, differences stem from the fact that muons can also couple to the photon, whereas neutrinos cannot. This effect is however negligible if the dilepton mass is close to the Z boson mass [38], and the distribution of the $Z(\nu\nu) + \text{jets}$ background can therefore be modelled using the dimuon control region in data. As the decay branching ratio of $Z \rightarrow \mu^+\mu^-$ is approximately 6 times smaller than that to neutrinos, the resulting statistical uncertainty on the $Z(\nu\nu) + \text{jets}$ template becomes a dominant systematic

uncertainty at large values of E_T^{miss} . A complementary approach is to additionally use events in data that have a high- p_T photon recoiling against jets to further constrain the $Z(\nu\nu) + \text{jets}$ background template [39]. At large boson transverse momentum, the kinematics of the $\gamma + \text{jets}$ and $Z + \text{jets}$ processes become similar as the finite mass of the Z boson becomes less relevant.

The dimuon control region is defined using the same selection as for the signal region, but removing the muon veto. Instead, exactly two muons with opposite charges are required. The leading p_T muon needs to be isolated and pass a tight identification and the mass of the dimuon system, $m_{\mu\mu}$, must be compatible with the Z boson mass, $60 < m_{\mu\mu} < 120$ GeV. The efficiency of the muon selection is measured in data and simulation using a tag-and-probe method. A scale-factor of 0.985 ± 0.010 is derived and applied twice (once per muon) to the simulated $Z + \text{jets}$ events passing the dimuon selection.

The photon control region consists of events which are selected by a trigger requiring an isolated photon with transverse momentum greater than 150 GeV. The selected events are required to have at least one photon with $p_T > 170$ GeV and $|\eta| < 2.5$, ignoring photons in the ECAL transition region, $1.44 < |\eta| < 1.56$. Additionally, the photons are required to pass a set of quality and isolation cuts designed to reduce the contribution from jets faking photons. A conversion safe electron veto is applied to remove Drell-Yan events. The efficiency of the selection is measured in data using a tag-and-probe method in $Z \rightarrow ee$ events and compared to that measured in simulation [40]. A scale-factor of 0.97 ± 0.01 is applied to simulated events passing the selection to account for the difference in the photon identification efficiency between data and simulation.

For correcting the $W + \text{jets}$ background, a single-muon control region is defined by selecting events with exactly one muon with p_T larger than 20 GeV. We additionally require that the event's transverse mass, calculated as,

$$m_T = \sqrt{2E_T^{\text{miss}} p_T^\mu (1 - \cos \phi)}, \quad (1)$$

where ϕ is the angle between the muon and E_T^{miss} vector in the transverse plane, satisfies $50 < m_T < 100$ GeV, selecting $W \rightarrow \mu\nu$ decays. As in the dimuon control region, the muon efficiency scale-factor is applied to simulated events passing the selection.

In both the dimuon, single-muon and photon control regions, the dimuon pair, single-muon or the photon's momentum are removed and the E_T^{miss} is recalculated yielding a distribution of fake E_T^{miss} . The difference in the distribution of fake E_T^{miss} between the observed data and that expected from simulation in the control regions is used to derive a correction for the $Z + \text{jets}$ and $W + \text{jets}$ backgrounds in the signal region.

5.1.2 Correcting the $V + \text{jets}$ E_T^{miss} spectra

The E_T^{miss} spectra of the $V + \text{jets}$ backgrounds is corrected for through the use of a likelihood fit, simultaneously across all bins in the three control regions. The expected number of events N_i in a given bin i of fake E_T^{miss} , for a particular event category, is given by,

$$N_i^{Z_{\mu\mu}|\gamma} = \frac{\mu_i^{Z \rightarrow \nu\nu}}{R_i^{Z|\gamma}}, \quad (2)$$

for the dimuon and photon control regions and

$$N_i^W = \frac{\mu_i^{W \rightarrow l\nu}}{R_i^W}, \quad (3)$$

for the single-muon control region, where $\mu^{Z \rightarrow \nu\nu}$ and $\mu^{W \rightarrow l\nu}$ are the free parameters of the likelihood fit representing the yields of $Z(\nu\nu) + \text{jets}$ and $W(l\nu) + \text{jets}$ in each bin of the signal region.

The transfer factors R_i^Z account for the ratio of $BR(Z \rightarrow \nu\nu)/BR(Z \rightarrow \mu^+\mu^-)$ and the muon efficiency times acceptance in the dimuon control region, while R_i^γ account for the ratio of differential cross-sections between the Z+jet and photon+jet processes and the efficiency times acceptance of the photon selection for the photon plus jet control region. These transfer factors are derived as the ratio of the number of $Z(\nu\nu) + \text{jets}$ events in the signal region to that of $\gamma + \text{jets}$ or $Z(\mu\mu) + \text{jets}$ events in the photon and dimuon control regions, from the simulation. The differential boson p_T cross-sections of photon and Z production are first corrected using NLO k-factors derived by comparing their p_T distributions in events generated at single parton level with Madgraph5_aMC@NLO [14], and subsequently showered, to the distributions produced at leading order before deriving the transfer factors.

For the single-muon control region, the transfer factors R_i^W account for the difference between the W+jets in the control region and the signal region due to the acceptance of the muon selection and lepton veto. These are derived from the expectation from simulated W+jets events in the signal region and in the control region.

The likelihood is defined for each event category as the product over Poisson likelihoods for each bin in fake E_T^{miss} , in each of the three control regions, as

$$\begin{aligned} \mathcal{L}_c(\mu^{c,Z \rightarrow \nu\nu}, \mu^{c,W \rightarrow l\nu}, \theta, \phi) = & \prod_i \text{Poisson} \left(d_i^{c,\gamma} | B_i^{c,\gamma}(\phi) + \frac{\mu_i^{c,Z \rightarrow \nu\nu}}{R_i^{c,\gamma}(\theta)} \right) \\ & \times \prod_i \text{Poisson} \left(d_i^{c,Z} | B_i^{c,Z}(\phi) + \frac{\mu_i^{c,Z \rightarrow \nu\nu}}{R_i^{c,Z}(\theta)} \right) \\ & \times \prod_i \text{Poisson} \left(d_i^{c,W} | B_i^{c,W}(\phi) + \frac{\mu_i^{c,W \rightarrow l\nu}}{R_i^{c,W}(\theta)} \right), \end{aligned} \quad (4)$$

where $d_i^{c,\gamma/Z/W}$ are the observed number of events in each bin of the photon, dimuon and single-muon control regions. The superscript “c” has been introduced to signify the components which are independent in each of the categories. The expected contributions from background processes in the dimuon, single-muon and photon control regions are denoted B^Z , B^W and B^γ respectively.

Systematic uncertainties are modelled as constrained nuisance parameters, θ , which allow for variation of the transfer factors, $R^{\gamma/Z/W}$, in the fit and are treated as fully correlated between event categories. These include theoretical uncertainties on the photon to Z differential cross-section ratio from renormalization and factorization scale uncertainties. Electroweak corrections to the ratio are not accounted for in the simulation. Such corrections have been derived independently and applied to the differential cross-section ratio. The full correction is also taken as an uncertainty on the ratio, which is of the order of 15% when the boson (Z or γ) p_T is around 1 TeV [41, 42]. This uncertainty is assumed to be uncorrelated across bins of E_T^{miss} in order to be conservative. Additionally, the uncertainty in the muon and photon selection efficiency scale-factors are included and fully correlated across the event categories. The uncertainty on the muon efficiency scale-factor is correlated between the single-muon and dimuon control regions.

B^γ is determined using a measurement of the purity of photon selection, as detailed in [40]. For photons with $p_T > 170$ GeV, the purity is 0.97 ± 0.01 . Simulation is used to determine B^Z and B^W , which are mostly from diboson production. A systematic uncertainty of 10% is included for the background normalization [43] and correlated between the single-muon and dimuon control regions. A larger systematic uncertainty was considered to cover electroweak corrections at higher E_T^{miss} but this was found not to impact the results. As with the uncertainties on the transfer-factors, the uncertainties on the backgrounds are incorporated as nuisance parameters ϕ . The full likelihood is then given by the product of \mathcal{L}_c over the three event categories with a Gaussian constraint term for each of the nuisance parameters.

The likelihood is maximised (fit) with respect to the free parameters $\mu^{c,Z \rightarrow \nu\nu}$, $\mu^{c,W \rightarrow l\nu}$ and the nuisance parameters θ and ϕ . The results of the fit are shown in Figure 6. The ratios of the values of $\mu_i^{c,Z \rightarrow \nu\nu}$ and $\mu_i^{c,W \rightarrow l\nu}$ that maximise the likelihood to the number of simulated $Z(\nu\nu) + \text{jets}$ and $W(l\nu) + \text{jets}$ events in each bin gives a per-bin re-weight that is applied to the simulated V+jets background events in the signal region.

These re-weighted events are then binned to provide E_T^{miss} templates for the two major backgrounds. The nuisance parameter uncertainties, as well as the statistical uncertainties on the correction function parameters themselves, are propagated as shape and normalization variations for the Z+jets and W+jets E_T^{miss} templates.

5.2 Other Backgrounds

The remaining backgrounds are expected to be much smaller than those from V+jets and are estimated directly from the simulation. Shape and normalization systematic uncertainties from the recoil corrections applied to these backgrounds are included to account for the uncertainty in the energy scale and resolution of jets. Additionally, a systematic uncertainty of 4% is included for the top backgrounds due to the uncertainty of the b-tagging efficiency for the b-jet veto in the resolved category. Systematic uncertainties of 7%, 10% and 50% are included for the top, diboson and QCD backgrounds respectively to account for the uncertainty in their production cross-sections. Finally, a systematic uncertainty of 2.6% in the luminosity measurement [44] is included for all of the MC derived backgrounds.

Table 1 gives a summary of the systematic uncertainties on the backgrounds estimation which are propagated to the calculation of the limits.

6 Results

The expected yields per bin of E_T^{miss} of all of the SM backgrounds, after the fit in the control regions, for each of the three event categories, are given in Tables 2, 3 and 4. The uncertainties given represent the sum in quadrature of the effect from each of the sources of systematic listed in Table 1 in each bin of E_T^{miss} . The correlations of these uncertainties between the different bins are however not reflected in the quoted numbers.

A second fit is performed, including the signal regions, assuming no signal is present. The backgrounds are allowed to vary within the systematic uncertainties listed in Table 1, accounting for any correlations between E_T^{miss} bins and between categories. The corresponding comparisons between data and background in the E_T^{miss} distributions, for each of the three categories, after this fit are shown in Figure 7.

Agreement between the expected SM backgrounds and data is observed at the percent level across the three categories. The local significance is calculated by constructing a signal model

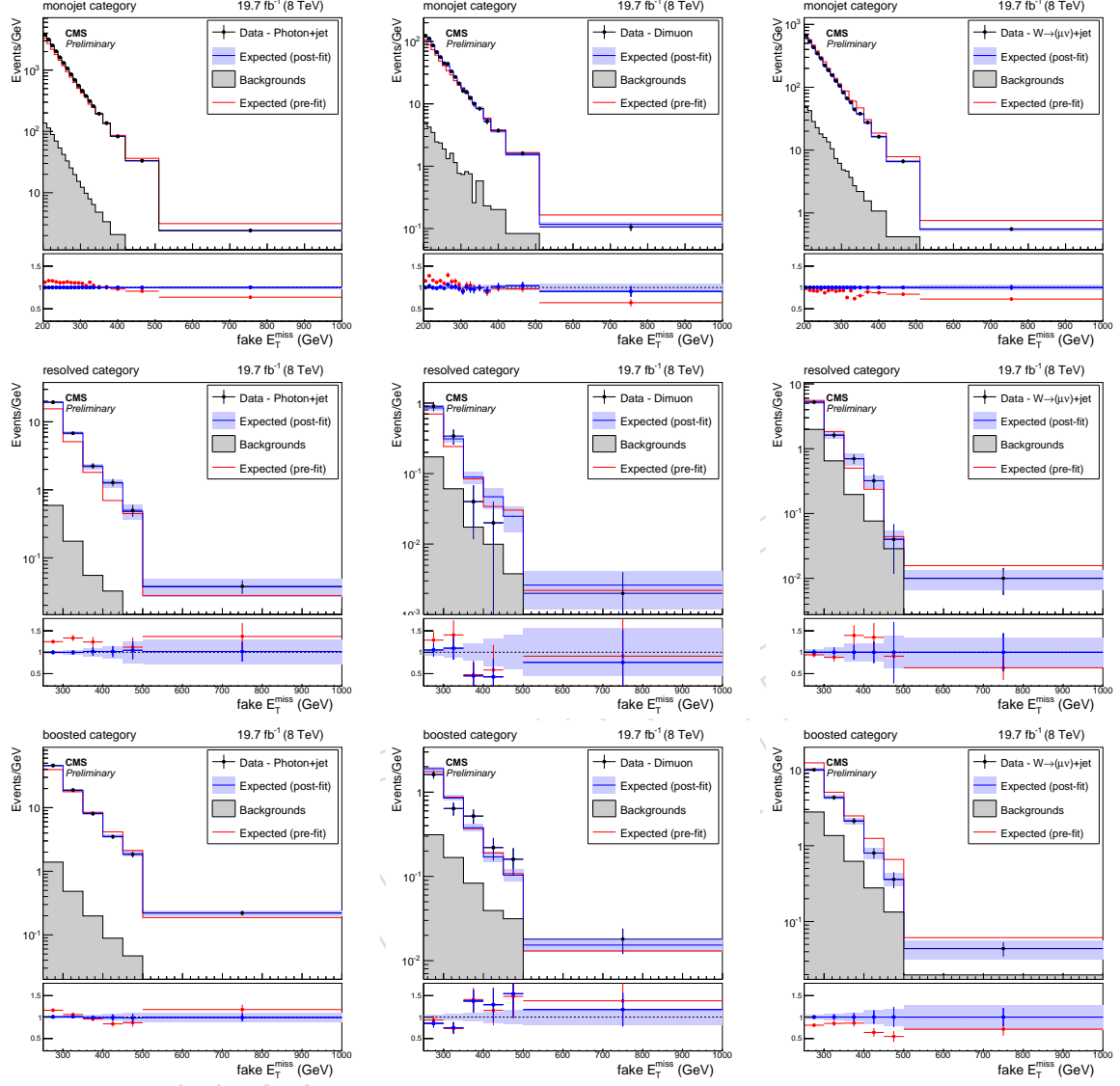


Figure 6: Expected and observed fake E_T^{miss} distributions in the photon (left), dimuon (middle) and single-muon (right) control regions after performing the simultaneous likelihood fit to the control regions. Each row, from top to bottom, shows the result of the fit in the monojet, resolved and boosted event categories respectively. The red line represents the expected distribution before fitting to the control regions, while the blue line shows the expectation after the fit. In the ratio, the blue and red points show the ratio of the observed data to the post-fit and pre-fit expectations respectively. The blue bands indicate the statistical and systematic uncertainties from the fit.

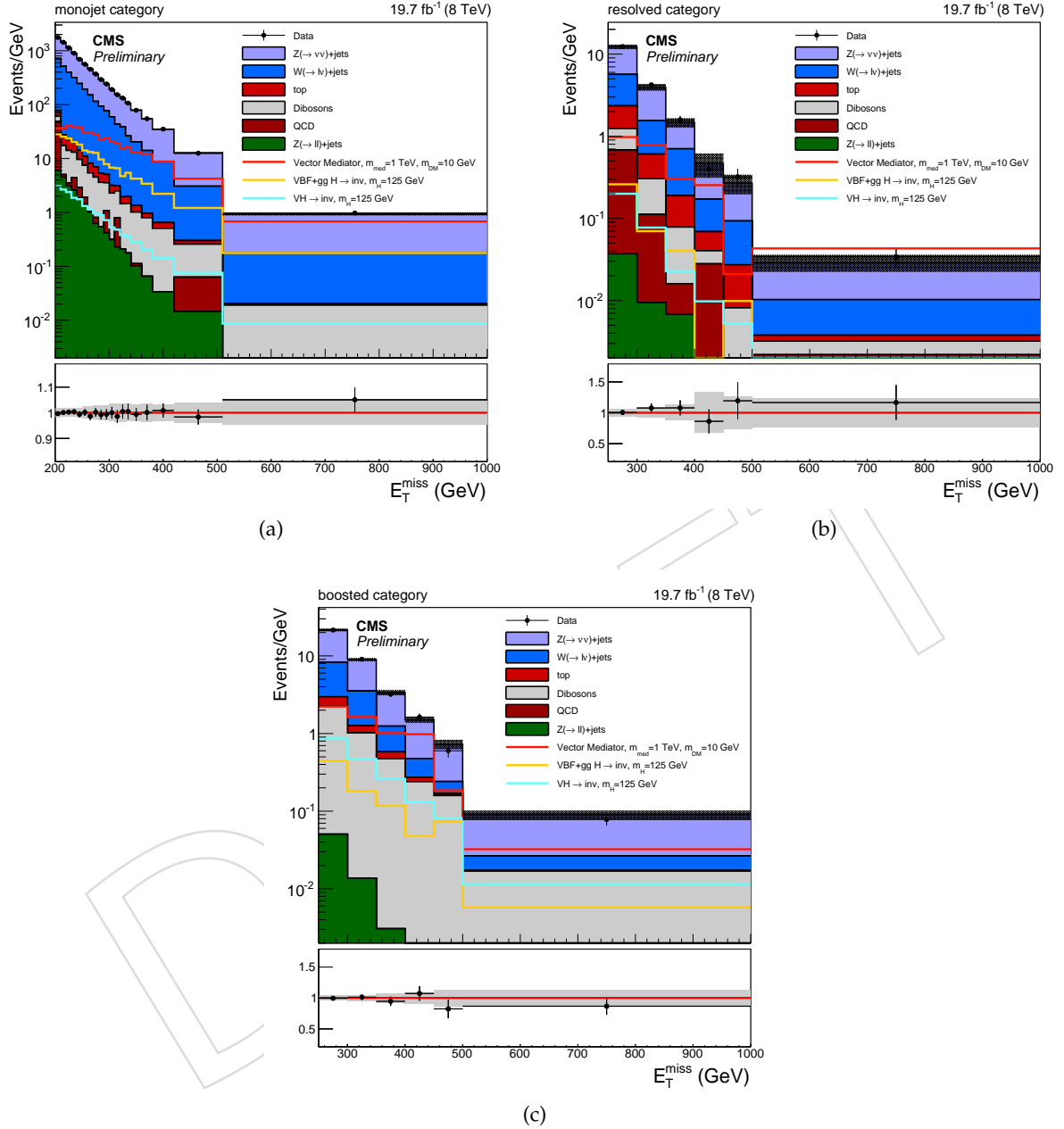


Figure 7: Post-fit distributions of E_T^{miss} expected from SM backgrounds and observed in data in the signal region. The expected distributions are evaluated after fitting to the observed data simultaneously across the monojet (a), resolved (b) and boosted (c) categories. The gray bands indicate the post-fit uncertainty on the background, assuming no signal. The expected distribution from a Higgs boson with mass 125 GeV is shown, assuming a 100% branching ratio to invisible particles, split into the contributions from vector boson fusion and gluon fusion (VBF+ggH) and associated vector boson production modes (VH).

Table 1: Systematic uncertainties and their relative effect on the expectation for the SM backgrounds.

Systematic Uncertainty	Process	Boosted	Resolved	Monojet
Control region fits [†]	$Z(\nu\nu) + \text{jets}$	6-20%	7.6-44%	2.5-9.5%
	$W(l\nu) + \text{jets}$	10.5-55%	14.5-320%	3.6-17%
Tau-id efficiency	$W(l\nu) + \text{jets}$	3.6%	3.6%	3.6%
V-tag efficiency [‡]	Dibosons, Top	10%,6%		
b-tag efficiency	Top	4%		
E_T^{miss} recoil	Dibosons	0.6%	2.8%	0.3%
	Top	1.1%	1.8%	1.3%
	$Z(l\bar{l}) + \text{jets}$	5.8%	9.4%	0.7%
$t\bar{t}$ norm	Top	7%	7%	7%
Dibosons norm	Dibosons	10%	10%	10%
QCD norm	QCD	50%	50%	50%
Luminosity	All except V+jets	2.6%	2.6%	2.6%

[†] The relevant components of the fit uncertainties relating to theory and muon/photon identification scale-factors in the control regions, described in Section 5.1, are included here and correlated between event categories. The numbers here indicate the range of the size of the uncertainties (the smallest to largest) in any E_T^{miss} bin due to these fits but should not be interpreted as the systematic uncertainty which is propagated to the signal extraction. For the boosted category, the uncertainty of 320% is simply the result of a small fitted yield in one of the bins of the single muon control region.

[‡] Uncertainty modeled as migration between the V-tagged (boosted and resolved) and monojet categories.

for which the signal events exist only in a single bin and comparing the likelihood of the background-only fit to a fit including that signal, allowing the signal yield to float freely. The largest local significance, calculated this way, in any of the bins across the three categories, is 1.9σ and corresponds to the excess seen in the last E_T^{miss} bin of the monojet category. Exclusion limits are set for a number of DM models as calculated with the CLs method [45] using a profile likelihood ratio as the test-statistic in which systematic uncertainties are modelled as nuisance parameters. For each signal hypothesis tested, upper limits are placed on the ratio of the signal cross-section to the predicted cross-section, denoted as $\mu = \sigma/\sigma_{TH}$.

7 DM Interpretations

The results are interpreted under a Higgs-boson model, in which the Higgs boson decays invisibly, and a set of simplified mediator models [25, 46–48], which are compatible with the recent recommendation of the LHC DM forum [12]. The limits obtained in the simplified models are compared to direct detection experiments. When doing so, the standard approaches to compute t-channel scattering are followed [48–51]. The approach outlined in [25] (see equation 1 to 6) is followed in which, for the scalar and pseudoscalar mediators, the couplings to quarks are assumed to be proportional to the corresponding Higgs Yukawa coupling ($g_{SM} = g_q m_q/\nu$, as mentioned in Section 3). In the vector and axial-vector cases the coupling, g_{SM} , is assumed to be a flavour universal gauge coupling. In all of the interpretations shown, it is assumed $g_q = 1$ for the spin-0 mediators and $g_{SM} = 1$ for the spin-1 mediators.

For vector and axial-vector mediators, spin-dependant (SD) and spin-independent (SI) DM-nucleon scattering cross-sections, under a simplified model assumption, have been previously calculated [11, 52] allowing for a direct mapping of limits expressed in the $m_{\text{MED}} - m_{\text{DM}}$ plane

Table 2: Expected yields of the standard model processes and their uncertainties per bin for the monojet category signal region after applying all corrections to the MC.

$E_T^{miss} \text{ bin (GeV)}$	Observed	Total Bkg	$Z(\rightarrow l\nu)\text{jets}$	top	QCD	$W(\rightarrow l\nu)\text{jets}$	Dibosons	$Z(\rightarrow \nu\nu)\text{jets}$
200 - 210	17547	18332.2 ± 598.0	59.8 ± 1.5	132.1 ± 11.3	479.3 ± 216.7	6771.6 ± 315.3	134.5 ± 13.5	10742.2 ± 274.3
210 - 220	14303	14500.1 ± 606.5	44.9 ± 1.2	103.6 ± 12.5	6.5 ± 3.0	4988.5 ± 235.3	111.5 ± 11.0	9234.4 ± 225.4
220 - 230	11343	11371.7 ± 395.6	31.5 ± 0.8	82.1 ± 7.3	4.4 ± 2.0	3832.1 ± 170.8	95.1 ± 9.6	7316.4 ± 189.8
230 - 240	8961	8942.9 ± 395.8	26.1 ± 0.7	62.0 ± 5.8	21.3 ± 9.6	3019.4 ± 159.2	77.9 ± 8.6	5727.5 ± 170.6
240 - 250	6920	7293.5 ± 333.3	18.6 ± 0.5	46.6 ± 4.4	12.0 ± 5.4	2470.0 ± 137.0	61.0 ± 6.1	4678.0 ± 150.1
250 - 260	5582	5670.9 ± 369.5	14.3 ± 0.4	34.2 ± 3.7	5.6 ± 2.5	1858.0 ± 116.8	50.1 ± 4.9	3702.5 ± 139.4
260 - 270	4517	4949.1 ± 318.4	10.2 ± 0.3	27.7 ± 2.3	0.2 ± 0.1	1579.2 ± 105.6	39.7 ± 4.2	3287.0 ± 125.0
270 - 280	3693	3741.1 ± 161.4	6.3 ± 0.2	25.0 ± 3.1	2.1 ± 1.0	1101.2 ± 70.6	33.5 ± 3.4	2567.8 ± 107.2
280 - 290	2907	3074.7 ± 181.5	5.4 ± 0.1	17.8 ± 1.9	0.0 ± 0.0	933.7 ± 70.9	28.1 ± 3.0	2085.3 ± 89.4
290 - 300	2406	2526.6 ± 170.1	4.2 ± 0.1	15.0 ± 3.6	7.7 ± 3.5	754.1 ± 58.3	21.9 ± 2.7	1721.1 ± 85.2
300 - 310	1902	1945.8 ± 156.1	3.1 ± 0.1	8.9 ± 1.6	0.0 ± 0.0	577.1 ± 50.6	17.7 ± 2.1	1336.6 ± 78.9
310 - 320	1523	1649.7 ± 109.6	2.3 ± 0.1	5.9 ± 2.2	6.6 ± 3.0	435.2 ± 43.2	15.5 ± 1.8	1181.6 ± 58.3
320 - 330	1316	1321.4 ± 91.5	2.1 ± 0.1	5.2 ± 1.3	0.0 ± 0.0	370.6 ± 44.4	11.0 ± 1.8	930.7 ± 53.1
330 - 340	1065	1069.7 ± 116.3	1.8 ± 0.0	4.9 ± 1.1	0.0 ± 0.0	246.0 ± 28.7	11.9 ± 1.8	803.5 ± 50.9
340 - 360	1571	1652.0 ± 109.4	2.0 ± 0.1	6.8 ± 1.2	0.2 ± 0.1	398.5 ± 38.5	16.4 ± 1.6	1225.2 ± 60.9
360 - 380	1091	1111.4 ± 148.6	1.3 ± 0.0	3.4 ± 0.4	0.0 ± 0.0	269.1 ± 30.5	13.3 ± 1.4	822.4 ± 53.3
380 - 420	1404	1387.1 ± 114.1	1.4 ± 0.0	5.5 ± 0.6	0.0 ± 0.0	324.4 ± 30.4	17.1 ± 1.7	1035.9 ± 65.9
420 - 510	1126	1238.9 ± 139.5	1.3 ± 0.0	3.9 ± 0.8	5.1 ± 2.3	266.9 ± 26.6	15.7 ± 1.6	943.4 ± 69.7
510 - 1000	476	413.0 ± 71.0	0.3 ± 0.0	0.6 ± 0.2	0.0 ± 0.0	72.1 ± 12.2	8.2 ± 0.8	330.4 ± 32.2

Table 3: Expected yields of the standard model processes and their uncertainties per bin for the resolved category signal region after applying all corrections to the MC.

$E_T^{miss} \text{ bin (GeV)}$	Observed	Total Bkg	$Z(\rightarrow ll)+\text{jets}$	top	QCD	$W(\rightarrow lv)+\text{jets}$	Dibosons	$Z(\rightarrow \nu\nu)+\text{jets}$
250 - 300	617	587.1 \pm 48.3	1.9 \pm 0.0	55.4 \pm 4.7	37.4 \pm 16.9	166.0 \pm 26.4	27.9 \pm 1.6	298.0 \pm 35.8
300 - 350	211	170.0 \pm 17.7	0.5 \pm 0.0	15.2 \pm 1.5	5.9 \pm 2.7	40.7 \pm 10.4	9.6 \pm 0.3	97.8 \pm 13.9
350 - 400	79	62.1 \pm 11.7	0.3 \pm 0.0	5.5 \pm 0.7	0.5 \pm 0.2	21.5 \pm 8.9	3.2 \pm 0.3	31.1 \pm 7.0
400 - 450	20	38.3 \pm 10.5	0.1 \pm 0.0	1.5 \pm 0.2	1.5 \pm 0.7	14.5 \pm 8.5	0.6 \pm 0.3	20.1 \pm 6.4
450 - 500	16	8.5 \pm 3.6	0.0 \pm 0.0	1.0 \pm 0.4	0.0 \pm 0.0	1.0 \pm 2.6	0.4 \pm 0.1	6.1 \pm 2.7
500 - 1000	17	11.6 \pm 3.5	0.0 \pm 0.0	0.3 \pm 0.2	1.3 \pm 0.6	2.6 \pm 1.7	0.5 \pm 0.0	6.9 \pm 3.0

Table 4: Expected yields of the standard model processes and their uncertainties per bin for the boosted category signal region after applying all corrections to the MC.

$E_T^{miss} \text{ bin (GeV)}$	Observed	Total Bkg	$Z(\rightarrow ll)+\text{jets}$	top	QCD	$W(\rightarrow lv)+\text{jets}$	Dibosons	$Z(\rightarrow \nu\nu)+\text{jets}$
250 - 300	1073	1103.0 \pm 63.4	2.5 \pm 0.0	35.4 \pm 3.7	0.0 \pm 0.0	278.8 \pm 32.5	103.2 \pm 14.6	682.5 \pm 40.1
300 - 350	453	445.7 \pm 33.9	0.7 \pm 0.0	12.7 \pm 1.3	0.0 \pm 0.0	114.3 \pm 19.6	46.5 \pm 6.9	271.4 \pm 22.8
350 - 400	160	184.0 \pm 18.1	0.2 \pm 0.0	5.6 \pm 1.0	0.0 \pm 0.0	38.3 \pm 8.7	22.2 \pm 3.3	117.4 \pm 12.8
400 - 450	81	72.1 \pm 28.9	0.0 \pm 0.0	1.5 \pm 0.8	0.0 \pm 0.0	9.8 \pm 3.4	11.0 \pm 1.8	49.7 \pm 7.3
450 - 500	30	44.3 \pm 6.6	0.0 \pm 0.0	0.5 \pm 0.1	0.0 \pm 0.0	5.0 \pm 2.6	7.4 \pm 1.1	31.2 \pm 6.1
500 - 1000	39	54.3 \pm 8.5	0.0 \pm 0.0	0.2 \pm 0.0	0.0 \pm 0.0	6.4 \pm 3.4	7.8 \pm 1.1	39.8 \pm 7.8

into limits expressed in terms of $\sigma_{\text{SI/SD}} - \text{DM}$ plane. For scalar interactions, the procedures outlined in [25] and [49–52] are used to calculate the spin-independent scattering cross-sections. Unlike the scalar, vector and axial-vector, the scattering amplitude of a pseudoscalar off a nucleus is strongly velocity dependent and vanishes in the non-relativistic limit thus the sensitivity in direct detection is greatly reduced. For the pseudoscalar scenario, indirect detection experiments can result in stronger bounds than direct detection experiments [53, 54]. The results of this analysis are interpreted in terms of upper limits on the DM pair-annihilation cross-section using the procedures outlined in [22, 25, 55].

For the vector and scalar mediator models, the limits are compared with the measurements by LUX [56–58] which currently provides the strongest bounds for $m_{\text{DM}} \gtrsim 6$ GeV. For axial-vector couplings, the limits are compared with the combined bounds of DM-proton-scattering limits from PICO-2L [59], while for the pseudoscalar case, the comparison is made with constraints from FermiLAT [60, 61]. The results are also compared, for all four types of mediators, to constraints obtained from the observed cosmological relic density of DM as determined from measurements of the cosmic microwave background by the WMAP and Planck experiments [62, 63]. The expected DM abundance is estimated, separately for each model, using a thermal freeze-out mechanism implemented in MadDM [64], and compared to the observed cold DM density $\Omega_c * h^2 = 0.12$ [65]. It is assumed that the simplified model hypothesised provides the only relevant BSM dynamics for DM interactions.

7.1 Invisible Higgs boson

Assuming SM production of the Higgs boson, gluon-fusion, vector-boson fusion and V-boson associated production are generated with a range of masses including 125 GeV. The p_T of the gluon-fusion component is corrected using an NNLO calculation of the differential cross-section which is NLL resummed calculated using HRES [66]. The production cross-sections for the four modes are taken from the recommendations of the LHC Higgs cross-section working group [67]. Uncertainties on the p_T spectrum of the gluon-fusion Higgs boson are included as shape variations, as well as theoretical uncertainties on the production cross-sections. These include QCD scale and PDF uncertainties on the theoretical cross-section at the level of 7% for the gluon fusion and 2% for the vector-boson fusion processes. Additionally, the theoretical uncertainties include migration and acceptance systematic uncertainties to cover potential mis-modelling of the jets. The dominant experimental systematic uncertainties included are the jet and E_T^{miss} scale and resolution uncertainties.

The simulated Higgs bosons are forced to decay exclusively to invisible particles so that upper limits on $\mu = \sigma \times BR(H \rightarrow \text{invisibles}) / \sigma_{\text{SM}}$ are calculated. Figure 8 shows the 95% confidence level (CL) upper limits on μ as a function of the hypothesized mass. The limits are shown combining the V-tagged categories only, where the associated-V production dominates and the full combination of all three categories. The kink in the limits for the full combination around 300 GeV is due to the monojet category where the gluon-fusion cross-section increases [24].

By assuming the SM cross-sections for the Higgs boson, the exclusion at 125 GeV is interpreted as an upper limit on the branching ratio of the Higgs to invisibles. The observed (expected) upper limit is $BR(H \rightarrow \text{invisibles}) < 0.53$ (0.62) at 95% CL when combining all three event categories.

7.2 Simplified Models

Simplified model results are presented scanning over mediator mass and DM mass for the different mediator models. For each of the simplified model interpretations, mediator masses

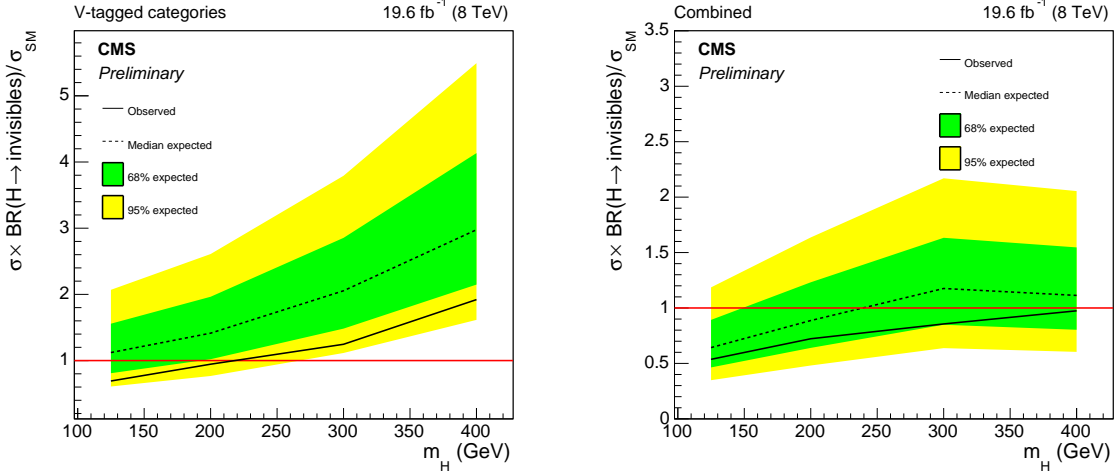


Figure 8: Expected (dashed) and observed (solid) upper limits on μ at the 95% CL as a function of the Higgs boson mass when combining the two V-tagged categories (left) and combining all three categories (right) .

ranging from 125 GeV to a mass of 5 TeV and DM masses of 1 GeV to 1 TeV are considered. The width is fixed to the minimum width assuming the mediator couples to standard model particles and the DM candidate. Events are generated for each point in a grid of mediator mass versus DM mass and showered using Pythia8 [15]. These generated samples are then used to re-weight the E_T^{miss} distributions of a smaller set of signal samples, generated in a coarser grid of mediator versus DM mass points, which have been passed through the full CMS simulation and reconstruction. This provides predictions of the E_T^{miss} spectrum at points where no fully simulated sample is available. The signal prediction for the simplified model interpretations is then taken as the sum of the contributions from the monojet and mono-V signatures in each of the three event categories.

Experimental systematic uncertainties, including jet and E_T^{miss} response and resolution, are included on the signal model when calculating the limits, while the theoretical systematic uncertainties on the inclusive cross-section (20% and 30% for the vector and axial-vector, and scalar and pseudoscalar models respectively) due to QCD scale and PDF uncertainties are instead added as additional contours to the exclusion limits. These uncertainties are chosen to be conservative across the full range in mediator mass.

Limits are calculated in terms of exclusion of regions in the $m_{\text{MED}} - m_{\text{DM}}$ plane, assuming the four different mediators, by determining the points for which $\mu \geq 1$ is excluded at 90% CL or more. Figure 9 shows the 90% CL exclusions for the vector, axial-vector, scalar and pseudoscalar mediator models. The 90% confidence level upper limit on the ratio of excluded cross-section to the predicted cross-section (μ_{up}), when assuming the mediator only couples to fermions, is shown by the blue color scale. These limits are obtained under the assumption that only the initial state partons and the DM particle contribute to the width of the mediator. For all models, the width is fixed under the minimum width constraint [9, 10, 12, 68]. For the vector mediator, the direct detection bounds dominate across most of the plane, while for the axial-vector, there is good complementarity between the direct detection limits and those from this analysis. Limits in the scalar mediator scenario are much weaker than those from direct detection for small dark-matter masses. Additional sensitivity is gained for larger mediator masses in this scenario above 350 GeV due to the rise in cross-section of the gluon fusion loop process above the $t\bar{t}$ threshold. In the pseudoscalar mediator scenario, the limits from this analysis exceed the reach in m_{MED} than those from FermiLAT.

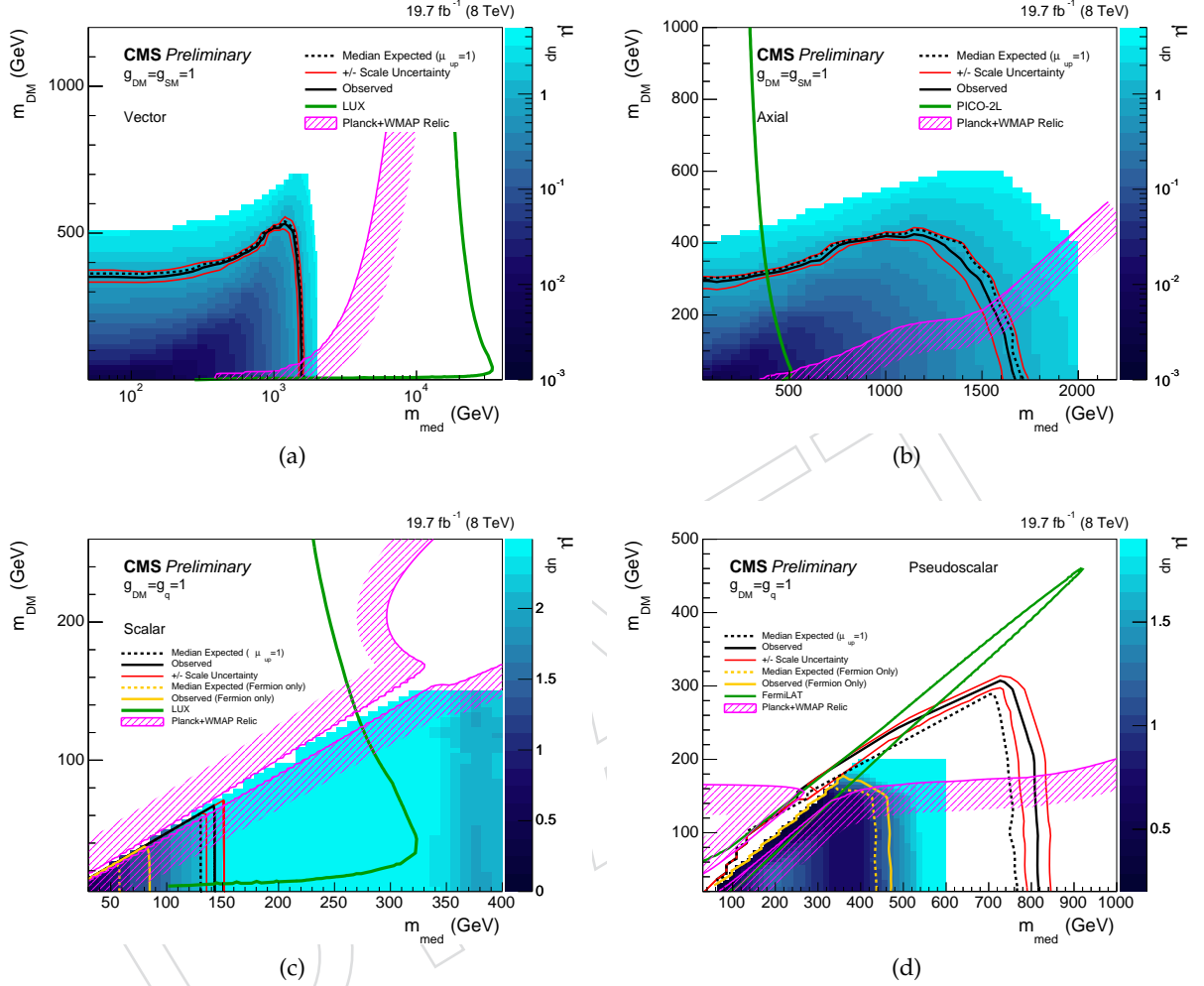


Figure 9: 90% CL Exclusion contours in the $m_{\text{med}} - m_{\text{DM}}$ plane assuming a vector (a), axial-vector (b), scalar (c), or pseudoscalar (d) mediator. The blue scale shows the 90% CL upper limit on the signal strength assuming the mediator only couples to fermions. For the scalar and pseudoscalar mediators, the exclusion contour assuming coupling only to fermions is explicitly shown in the orange line. The white region shows model points which were not tested when assuming coupling only to fermions and are not expected to be excluded by this analysis under this assumption. The excluded region is to the bottom-left of the contours shown in all cases except for that from the relic density as indicated by the shading. In all of the mediator models, a minimum width is assumed.

Figures 10a, 10b and 10c show the same exclusion contours, this time translated into the plane of $m_{\text{DM}} - \sigma_{\text{SI/SD}}$, where $\sigma_{\text{SI/SD}}$ are the spin-independent/dependant (vector and scalar/axial-vector) DM-nucleon scattering cross-sections. These representations allow for a more direct comparison with limits from the direct detection experiments which typically set upper limits on these cross-sections [47, 69]. It should be noted that the limits set from this analysis are only valid under the simplified model considered, and in particular assuming $g_{\text{DM}} = g_{\text{SM}} = 1$. For the scalar model, it is assumed that only heavy quarks (top and bottom) contribute. Such a choice limits the sensitivity for direct detection, however it allows for direct comparison between collider and direct detection without an additional assumption on the light quark couplings [69]. For the vector and scalar mediator models, direct-detection limits are stronger than those obtained in this analysis except in the scenario where the dark matter mass is less than around 6 GeV while for the axial-vector mediator model, the limits obtained in this analysis dominate up to around $m_{\text{DM}} = 300$ GeV.

For pseudoscalar interactions, direct detection bounds are strongly velocity suppressed. The most appropriate comparison is therefore to the most sensitive bounds from indirect detection from FermiLAT [70]. These limits apply to the scenario in which dark matter is annihilated in the center of a galaxy producing a γ ray signature. The observed excess in this production has led to speculations that dark matter annihilation is mediated by a light pseudoscalar. The production mechanism for these γ rays can be interpreted under dark matter annihilation to b-quarks allowing for direct comparison limits from this analysis [22, 25, 55]. Figure 10d shows the exclusion contours assuming pseudoscalar mediation in the plane of DM pair annihilation cross-section versus m_{DM} . As in the scalar case, for the pseudoscalar model, it is assumed that only heavy quarks contribute in the production of the mediator. For the interpretation of the limits in the annihilation cross-section, it is however assumed that the mediator only decays to b-quark pairs. As in all cases, the interpretations are given assuming a Dirac-fermion DM particle. The 68% CL preferred regions in this plane assuming the annihilation of DM pairs to light-quarks (qq), tau or bottom pairs, using data from FermiLAT [71], are shown as solid colour regions. Under the simplified model used, all of these regions are excluded by this analysis.

8 Summary

A search has been presented for an excess of events with a high energy jet in association with a large missing transverse momentum in a data sample of proton-proton interactions at centre-of-mass energy of 8 TeV. The data correspond to an integrated luminosity of 19.7 fb^{-1} collected by the CMS detector at the LHC. Sensitivity to mono-V models is achieved by tagging events consistent with the jet originating from a hadronically decaying vector boson. No significant deviation from the expectation from SM backgrounds is observed in the $E_{\text{T}}^{\text{miss}}$ distributions. A 95% CL observed (expected) upper limit of 0.53 (0.62) is obtained on the branching ratio of a SM Higgs boson with a mass of 125 GeV decaying to invisible particles. The search is also interpreted in terms of DM production to place constraints on the parameter space of the simplified models considered. From these, constraints are placed on dark-matter-nucleon scattering cross-sections using both spin-dependent and spin-independent interactions.

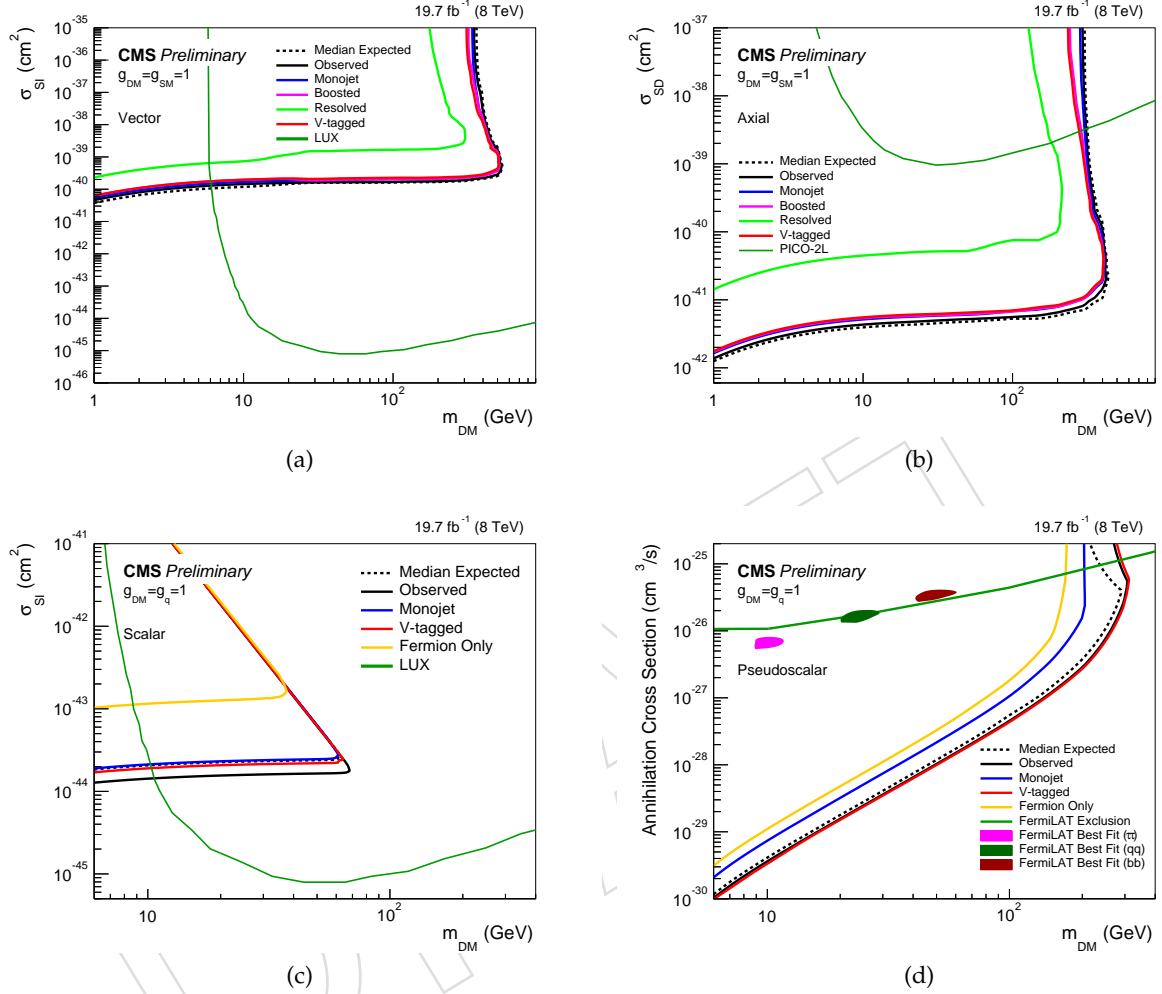


Figure 10: 90% CL Exclusion contours in the $m_{\text{DM}} - \sigma_{\text{DM}}$ plane assuming a vector (a), axial-vector (b), scalar (c), or pseudoscalar (d) mediator. For the scalar and pseudoscalar case, the orange line shows the exclusion contours assuming the mediator only couples to fermions. The excluded region in all plots is to the top left of the contours shown. In the vector and axial-vector scenarios, limits are shown independently for monojet, boosted and resolved categories. The partial combination of the “V-tagged” categories (resolved and boosted) categories is shown for which the boosted category provides the dominant contribution. In all of the mediator models, a minimum width is assumed. For the pseudo-scalar, 68% CL preferred regions, using data from FermiLAT, for DM annihilation to light-quarks (qq), tau pairs ($\tau\tau$) and bottom-quark pairs (bb) are shown by the solid green, pink and brown coloured regions respectively.

References

- [1] CMS Collaboration, “Search for dark matter, extra dimensions, and unparticles in monojet events in protonproton collisions at $\sqrt{s} = 8$ TeV”, *Eur.Phys.J.* **C75** (2015), no. 5, 235, doi:10.1140/epjc/s10052-015-3451-4, arXiv:1408.3583.
- [2] ATLAS Collaboration, “Search for new phenomena in final states with an energetic jet and large missing transverse momentum in pp collisions at $\sqrt{s} = 8$ TeV with the ATLAS detector”, arXiv:1502.01518.
- [3] CMS Collaboration, “Search for physics beyond the standard model in final states with a lepton and missing transverse energy in proton-proton collisions at $\sqrt{s} = 8$ TeV”, *Phys.Rev.* **D91** (2015), no. 9, 092005, doi:10.1103/PhysRevD.91.092005, arXiv:1408.2745.
- [4] CMS Collaboration, “Search for invisible decays of Higgs bosons in the vector boson fusion and associated ZH production modes”, *Eur.Phys.J.* **C74** (2014), no. 8, 2980, arXiv:1404.1344.
- [5] ATLAS Collaboration, “Search for dark matter in events with a Z boson and missing transverse momentum in pp collisions at $\sqrt{s}=8$ TeV with the ATLAS detector”, *Phys. Rev.* **D90** (2014), no. 1, 012004, doi:10.1103/PhysRevD.90.012004, arXiv:1404.0051.
- [6] ATLAS Collaboration, “Search for dark matter in events with a hadronically decaying W or Z boson and missing transverse momentum in pp collisions at $\sqrt{s} = 8$ TeV with the ATLAS detector”, *Phys. Rev. Lett.* **112** (2014), no. 4, 041802, doi:10.1103/PhysRevLett.112.041802, arXiv:1309.4017.
- [7] ATLAS Collaboration, “Search for new particles in events with one lepton and missing transverse momentum in pp collisions at $\sqrt{s} = 8$ TeV with the ATLAS detector”, *JHEP* **09** (2014) 037, doi:10.1007/JHEP09(2014)037, arXiv:1407.7494.
- [8] Feng, J. *et al.*, “Isospin-Violating Dark Matter”, (2011). arXiv:1102.4331.
- [9] P. J. Fox, R. Harnik, J. Kopp, and Y. Tsai, “Missing Energy Signatures of Dark Matter at the LHC”, *Phys.Rev.* **D85** (2012) 056011, arXiv:1109.4398.
- [10] Busoni, G. *et al.*, “On the Validity of the Effective Field Theory for Dark Matter Searches at the LHC”, *Phys. Lett. B* **728C** (2014) 412–421.
- [11] O. Buchmueller, M. J. Dolan, and C. McCabe, “Beyond Effective Field Theory for Dark Matter Searches at the LHC”, *JHEP* **1401** (2014) 025, arXiv:1308.6799.
- [12] D. Abercrombie et al., “Dark Matter Benchmark Models for Early LHC Run-2 Searches: Report of the ATLAS/CMS Dark Matter Forum”, arXiv:1507.00966.
- [13] CMS Collaboration, “The CMS experiment at the CERN LHC”, *JINST* **3** (2008) S08004.
- [14] J. Alwall et al., “The automated computation of tree-level and next-to-leading order differential cross sections, and their matching to parton shower simulations”, *JHEP* **1407** (2014) 079, arXiv:1405.0301.
- [15] T. Sjöstrand, S. Mrenna, and P. Skands, “PYTHIA 6.4 physics and manual”, *JHEP* **05** (2006) 026, arXiv:hep-ph/0603175.

- [16] M. L. Mangano, M. Moretti, F. Piccinini, and M. Treccani, “Matching matrix elements and shower evolution for top-quark production in hadronic collisions”, *JHEP* **0701** (2007) 013, [arXiv:hep-ph/0611129](#).
- [17] C. Oleari, “The POWHEG BOX”, *Nuclear Physics B Proceedings Supplements* **205** (August, 2010) 36–41, [arXiv:1007.3893](#).
- [18] S. Agostinelli, J. Allison, K. Amako et al., “Geant4 - a simulation toolkit”, *Nuclear Instruments and Methods in Physics Research Section A: Accelerators, Spectrometers, Detectors and Associated Equipment* **506** (2003), no. 3, 250 – 303.
- [19] CMS Collaboration, “MET performance in 8 TeV data”, Technical Report CMS-PAS-JME-12-002, CERN, Geneva, 2013.
- [20] L. Basso, A. Belyaev, S. Moretti, and C. H. Shepherd-Themistocleous, “Phenomenology of the minimal B-L extension of the Standard model: Z' and neutrinos”, *Phys.Rev.* **D80** (2009) 055030, [doi:10.1103/PhysRevD.80.055030](#), [arXiv:0812.4313](#).
- [21] J. M. Campbell and R. K. Ellis, “MCFM for the Tevatron and the LHC”, *Nucl. Phys. Proc. Suppl.* **205-206** (2010) 10–15.
- [22] M. R. Buckley, D. Feld, and D. Goncalves, “Scalar Simplified Models for Dark Matter”, [arXiv:1410.6497](#).
- [23] I. Anderson et al., “Constraining anomalous HVV interactions at proton and lepton colliders”, *Phys.Rev.* **D89** (2014), no. 3, 035007, [arXiv:1309.4819](#).
- [24] LHC Higgs Cross Section Working Group Collaboration, “Handbook of LHC Higgs Cross Sections: 3. Higgs Properties”, [arXiv:1307.1347](#).
- [25] P. Harris, V. V. Khoze, M. Spannowsky, and C. Williams, “Constraining dark sectors at colliders: Beyond the effective theory approach”, *Phys. Rev. D* **91** (Mar, 2015) 055009, [doi:10.1103/PhysRevD.91.055009](#).
- [26] CMS Collaboration, “Search for invisible Higgs produced in association with a Z boson”, Technical Report CMS-PAS-HIG-13-018, CERN, Geneva, 2013.
- [27] M. Cacciari, G. P. Salam, and G. Soyez, “The Anti-k(t) jet clustering algorithm”, **04** (2008) 063, [doi:10.1088/1748-0221/6/11/P11002](#), [arXiv:1107.4277](#).
- [28] CMS Collaboration, “A Cambridge-Aachen (C-A) based Jet Algorithm for boosted top-jet tagging”, Technical Report CMS-PAS-JME-09-001, CERN, 2009. Geneva, Jul, 2009.
- [29] CMS Collaboration, “Determination of jet energy calibration and transverse momentum resolution in CMS”, *Journal of Instrumentation* **6** (November, 2011) 11002, [doi:10.1088/1748-0221/6/11/P11002](#), [arXiv:1107.4277](#).
- [30] CMS Collaboration, “Particle-Flow Event Reconstruction in CMS and Performance for Jets, Taus, and MET”, Technical Report CMS-PAS-PFT-09-001, CERN, 2009. Geneva, Apr, 2009.
- [31] J. Thaler and K. Van Tilburg, “Identifying boosted objects with N -subjettiness”, *JHEP* **03** (2011) 015, [arXiv:1011.2268](#).
- [32] J. Thaler and K. Van Tilburg, “Maximizing boosted top identification by minimizing N -subjettiness”, *JHEP* **02** (2012) 093, [arXiv:1108.2701](#).

- [33] S. D. Ellis, C. K. Vermilion, and J. R. Walsh, “Recombination Algorithms and Jet Substructure: Pruning as a Tool for Heavy Particle Searches”, *Phys.Rev.* **D81** (2010) 094023, [arXiv:0912.0033](#).
- [34] CMS Collaboration, “V Tagging Observables and Correlations”, CMS Physics Analysis Summary CMS-PAS-JME-14-002, 2014.
- [35] J. Gallicchio and M. D. Schwartz, “Seeing in Color: Jet Superstructure”, *Phys.Rev.Lett.* **105** (2010) 022001, [arXiv:1001.5027](#).
- [36] E. Izaguirre, B. Shuve, and I. Yavin, “Improving Identification of Dijet Resonances at Hadron Colliders”, *Phys.Rev.Lett.* **114** (2015), no. 4, 041802, [doi:10.1103/PhysRevLett.114.041802](#), [arXiv:1407.7037](#).
- [37] CMS Collaboration, “Identification of b-quark jets with the CMS experiment”, *JINST* **8** (2013) P04013, [arXiv:1211.4462](#).
- [38] CMS Collaboration, “Measurement of inclusive W and Z boson production cross sections in pp collisions at $\sqrt{s} = 8$ TeV”, *Phys.Rev.Lett.* **112** (2014) 191802, [arXiv:1402.0923](#).
- [39] CMS Collaboration, “Data-Driven Estimation of the Invisible Z Background to the SUSY MET Plus Jets Search”, Technical Report CMS-PAS-SUS-08-002, CERN, Geneva, 2008.
- [40] CMS Collaboration, “Performance of photon reconstruction and identification with the CMS detector in proton-proton collisions at $\sqrt{s} = 8$ TeV”, [arXiv:1502.02702](#).
- [41] J. H. Kuhn, A. Kulesza, S. Pozzorini, and M. Schulze, “Electroweak corrections to hadronic photon production at large transverse momenta”, *JHEP* **0603** (2006) 059, [arXiv:hep-ph/0508253](#).
- [42] S. Kallweit et al., “NLO QCD+EW automation and precise predictions for V+multijet production”, in *50th Rencontres de Moriond on QCD and High Energy Interactions La Thuile, Italy, March 21-28, 2015*. 2015. [arXiv:1505.05704](#).
- [43] CMS Collaboration, “Measurement of the $pp \rightarrow ZZ$ production cross section and constraints on anomalous triple gauge couplings in four-lepton final states at $\sqrt{s} = 8$ TeV”, *Phys.Lett.* **B740** (2015) 250–272, [doi:10.1016/j.physletb.2014.11.059](#), [arXiv:1406.0113](#).
- [44] CMS Collaboration, “CMS Luminosity Based on Pixel Cluster Counting - Summer 2013 Update”, Technical Report CMS-PAS-LUM-13-001, CERN, Geneva, 2013.
- [45] A. L. Read, “Presentation of search results: the CLs technique”, *Journal of Physics G: Nuclear and Particle Physics* **28** (2002), no. 10, 2693.
- [46] J. Abdallah et al., “Simplified Models for Dark Matter and Missing Energy Searches at the LHC”, [arXiv:1409.2893](#).
- [47] S. Malik et al., “Interplay and Characterization of Dark Matter Searches at Colliders and in Direct Detection Experiments”, [arXiv:1409.4075](#).
- [48] O. Buchmueller, M. J. Dolan, S. A. Malik, and C. McCabe, “Characterising dark matter searches at colliders and direct detection experiments: Vector mediators”, *JHEP* **01** (2015) 037, [doi:10.1007/JHEP01\(2015\)037](#), [arXiv:1407.8257](#).

- [49] A. Kurylov and M. Kamionkowski, “Generalized analysis of weakly interacting massive particle searches”, *Phys.Rev.* **D69** (2004) 063503, [arXiv:hep-ph/0307185](#).
- [50] J. Hisano, K. Ishiwata, and N. Nagata, “Gluon contribution to the dark matter direct detection”, *Phys.Rev.* **D82** (2010) 115007, [arXiv:1007.2601](#).
- [51] K. Cheung, C.-T. Lu, P.-Y. Tseng, and T.-C. Yuan, “Collider Constraints on the Dark Matter Interpretation of the CDMS II Results”, *ArXiv e-prints* (July, 2013) [arXiv:1308.0067](#).
- [52] H.-Y. Cheng and C.-W. Chiang, “Revisiting scalar and pseudoscalar couplings with nucleons”, *Journal of High Energy Physics* **7** (July, 2012) 9, [arXiv:1202.1292](#).
- [53] J.-M. Zheng et al., “Constraining the interaction strength between dark matter and visible matter: I. fermionic dark matter”, *Nucl.Phys.* **B854** (2012) 350–374, [arXiv:1012.2022](#).
- [54] C. Boehm et al., “Extended gamma-ray emission from Coy Dark Matter”, *JCAP* **1405** (2014) 009, [arXiv:1401.6458](#).
- [55] O. Buchmueller, S. A. Malik, C. McCabe, and B. Penning, “Constraining the Fermi-LAT excess with multi-jet plus MET collider searches”, [arXiv:1505.07826](#).
- [56] LUX Collaboration, “The Large Underground Xenon (LUX) Experiment”, *Nucl.Instrum.Meth.* **A704** (2013) 111–126, [arXiv:1211.3788](#).
- [57] LUX Collaboration, “First results from the LUX dark matter experiment at the Sanford Underground Research Facility”, *Phys.Rev.Lett.* **112** (2014), no. 9, 091303, [arXiv:1310.8214](#).
- [58] LUX Collaboration, “A Detailed Look at the First Results from the Large Underground Xenon (LUX) Dark Matter Experiment”, [arXiv:1402.3731](#).
- [59] PICO Collaboration, “Dark Matter Search Results from the PICO-2L C₃F₈ Bubble Chamber”, *Phys. Rev. Lett.* **114** (2015), no. 23, 231302, [doi:10.1103/PhysRevLett.114.231302](#), [arXiv:1503.00008](#).
- [60] Fermi-LAT Collaboration, “Constraining Dark Matter Models from a Combined Analysis of Milky Way Satellites with the Fermi Large Area Telescope”, *Phys.Rev.Lett.* **107** (2011) 241302, [arXiv:1108.3546](#).
- [61] Fermi-LAT Collaboration, “Observations of Milky Way Dwarf Spheroidal galaxies with the Fermi-LAT detector and constraints on Dark Matter models”, *Astrophys.J.* **712** (2010) 147–158, [arXiv:1001.4531](#).
- [62] WMAP Collaboration, “The Microwave Anisotropy Probe (MAP) mission”, *Astrophys.J.* **583** (2003) 1–23, [doi:10.1086/345346](#), [arXiv:astro-ph/0301158](#).
- [63] Planck Collaboration, “The Scientific programme of Planck”, [arXiv:astro-ph/0604069](#).
- [64] M. Backovic, K. Kong, and M. McCaskey, “MadDM v.1.0: Computation of Dark Matter Relic Abundance Using MadGraph5”, *Physics of the Dark Universe* **5-6** (2014) 18–28, [doi:10.1016/j.dark.2014.04.001](#), [arXiv:1308.4955](#).
- [65] Planck Collaboration, “Planck 2013 results. XVI. Cosmological parameters”, *Astron.Astrophys.* **571** (2014) A16, [doi:10.1051/0004-6361/201321591](#), [arXiv:1303.5076](#).

- [66] D. de Florian, G. Ferrera, M. Grazzini, and D. Tommasini, “Higgs boson production at the LHC: transverse momentum resummation effects in the $H \rightarrow 2\gamma$, $H \rightarrow WW \rightarrow l\nu l\nu$ and $H \rightarrow ZZ \rightarrow 4l$ decay modes”, *JHEP* **1206** (2012) 132, doi:10.1007/JHEP06(2012)132, arXiv:1203.6321.
- [67] LHC Higgs Cross Section Working Group Collaboration, “Handbook of LHC Higgs Cross Sections: 3. Higgs Properties: Report of the LHC Higgs Cross Section Working Group”, Technical Report arXiv:1307.1347. CERN-2013-004, Geneva, 2013.
- [68] H. An, X. Ji, and L.-T. Wang, “Light Dark Matter and Z' Dark Force at Colliders”, *JHEP* **07** (2012) 182, doi:10.1007/JHEP07(2012)182, arXiv:1202.2894.
- [69] P. Harris, V. V. Khoze, M. Spannowsky, and C. Williams, “Closing up on Dark Sectors at Colliders: from 14 to 100 TeV”, arXiv:1509.02904.
- [70] Fermi-LAT Collaboration, “Searching for Dark Matter Annihilation from Milky Way Dwarf Spheroidal Galaxies with Six Years of Fermi-LAT Data”, *Submitted to PRL* (2015) arXiv:1503.02641.
- [71] F. Calore, I. Cholis, C. McCabe, and C. Weniger, “A Tale of Tails: Dark Matter Interpretations of the Fermi GeV Excess in Light of Background Model Systematics”, *Phys. Rev. D* **91** (2015), no. 6, 063003, doi:10.1103/PhysRevD.91.063003, arXiv:1411.4647.